**ORIGINAL RESEARCH**

# Green and chemical-engineered CuFe$_2$O$_4$: characterization, cyclic voltammetry, photocatalytic and photoluminescent investigation for multifunctional applications

B. S. Surendra[1] · M. Veerabhdraswamy[2] · K. S. Anantharaju[3] · H. P. Nagaswarupa[1] · S. C. Prashantha[1]

## Abstract

CuFe$_2$O$_4$ nanoparticles (CNPs) with cubic and tetragonal spinel structures were synthesized by Jatropha oil-assisted green combustion route (GCR) and urea-assisted chemical combustion route (CCR) and well-characterized. The photocatalytic activity of CNPs prepared via GCR and CCR showed 96 and 83% sunlight degradation of Malachite green (MG) dye, respectively. Electrochemical properties of CNPs were studied by means of Cyclic Voltammetry (CV) and electrochemical impedance spectroscopy (EIS). The current research work pledges to provide some novel insights into the design of material for multifunctional long-term applications for environmental clean-up.

✉ B. S. Surendra
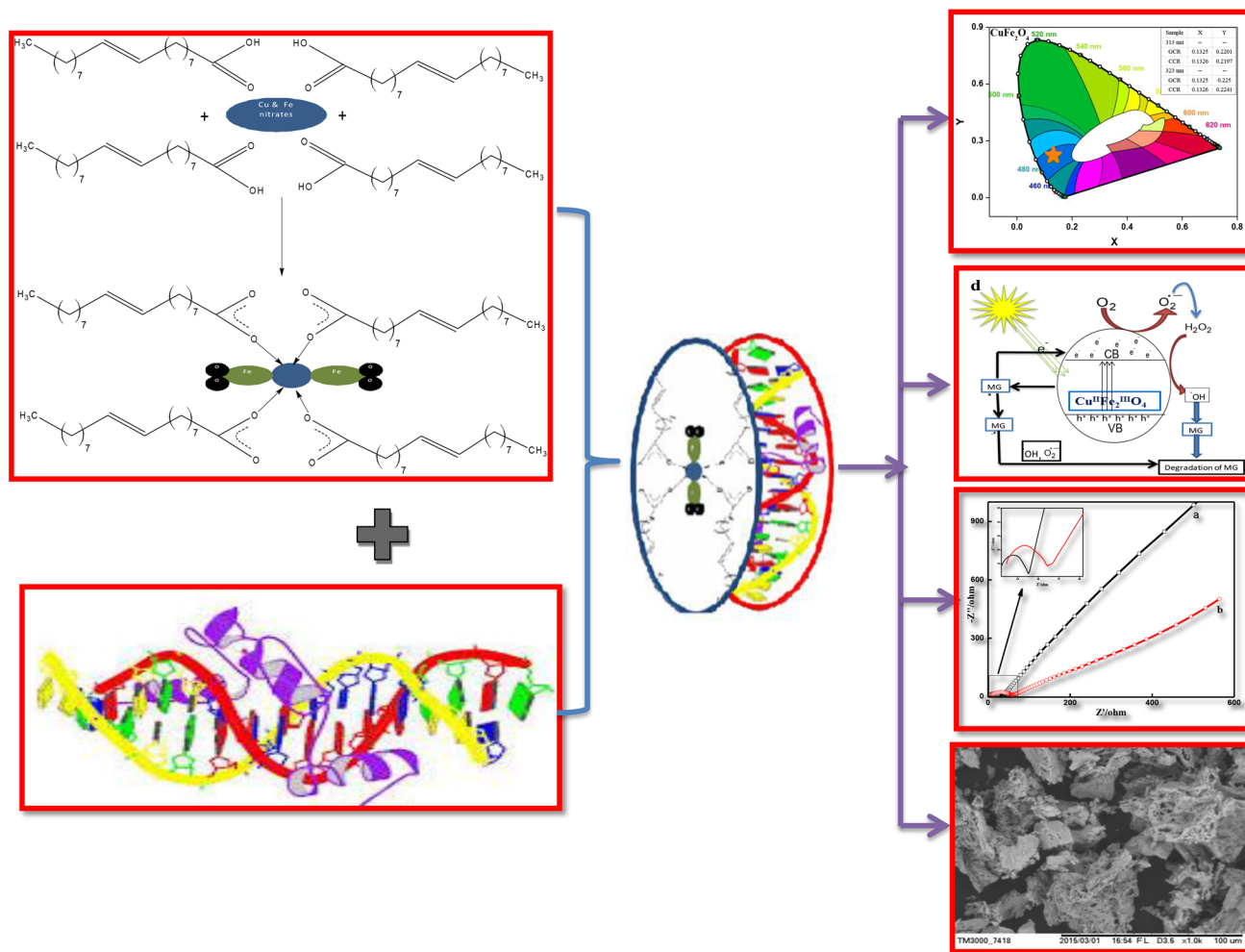 surendramysore2010@gmail.com

1 Department of Chemistry, East West Institute of Technology, Bengaluru 560 091, India

2 Department of Chemistry, PES Institute of Technology, Bengaluru 560 085, India

3 Department of Chemistry, Dayananda Sagar College of Engineering, Bengaluru 560078, India

Springer

**Graphical Abstract**



**Keywords** $CuFe_2O_4$ · GCR · Oxygen vacancies · Photoluminescence · CV and EIS · Photocatalysis

# Introduction

Biomass is the most abundant energy resource, significant energy feedstock and substitute to fossil fuels. It includes edible or non-edible plants which are essentially utilized as source for the production of biodiesel [1]. The non-edible plant seeds such as Jatropha, Neem, Pongamia, and Simarouba play a vital role in the production of biodiesel [2–5]. In general, 50–60% of the oil content present in seeds (kernels) was extracted from mechanical expeller and the remaining residue matter is also called seed cake, which contains little oil, proteins, carbohydrates, fiber and inorganic compounds [6, 7].

Nowadays waste water from different industries and laboratories creates a lot of problems to the environment due to some unwanted contaminants such as herbicides, azo dyes, and pesticides. Mainly the dye discharged into water from industries is very much toxic to microorganisms, aquatic life and human habitats [8–12]. Most of the semiconductor photocatalysts used for the treatment of organic pollutant can utilize only ultraviolet radiations due to their band gap values (> 3.1 eV) [13]. However, we need to develop a photo catalyst that efficiently extends visible light response in catalytic activity for ecological remediation which has become a large task and most dynamic research issues in photocatalytic activity [14–16]. In addition, there will be substantial cost savings when the suspended ultrafine photocatalyst can be reused again and again after degradation and is possible with magnetic catalysts [4]. In these regards, spinel ferrites $MFe_2O_4$ ($M$ = Mn, Zn, Ni, Cu, etc.) and their related structures have been researched for their photocatalysis and magnetic properties [17–20]. Unlike $TiO_2$ and ZnO, ferrites in nano size offer a benefit of displaying an

attractive optical absorption for low-energy photons (~ 2 eV) and showing the well-suited electronic structure attractive for photocatalytic activities. Also, ferrite nanoparticles have shown key attention due to their technological significance in high-density magnetic storage, delivery, gas sensors, etc. [21, 22]. The material that possesses properties such as good stability, high reactivity and capability to be magnetically separated can be applied in a various areas. In the present investigation, $CuFe_2O_4$ photocatalysts were fabricated by different routes (GCR and CCR), well characterized by various techniques and used for multifunctional applications.

## Materials and methods

### Jatropha oil extraction

Extraction of Jatropha oil was done by Soxhlet extraction method [23] using methanol as a solvent (boiling point of 60 °C), run down the process using heating mantle till up to 45 cycles at 70 °C followed by distillation of solvent and finally crude oil was collected. Composition of extracted Jatropha oil was analyzed using BTH/QL1/161 instrument and the details are given in the Table 1.

### Synthesis of $CuFe_2O_4$

In GCR, the stoichiometric quantities of analytic-grade Cu $(NO_3)_2.3H_2O$ and Fe $(NO_3)_3.9H_2O$ were used as starting materials and optimum amount of extracted Jatropha oil was used as a green fuel. These chemicals were taken in a

crucible with small quantity of double distilled water and magnetic stirrer, mixed thoroughly to attain homogeneity and placed in a muffle furnace maintained at 450 ± 10 °C. The mixture boils in less than 5 min, catches fire at one spot and slowly spread throughout the reaction mixture. Highly porous brownish black final product was obtained. However, in CCR method, stoichiometric amounts of urea are used as a fuel along with metal nitrates and the same procedure is followed to get the final product. The flow chart for the synthesis of $CuFe_2O_4$ by GCR and CCR were shown in Fig. 1.

## Characterization

The phase investigation was carried out in Shimadzu PXRD (Powder X-ray diffractometer) using nickel filter in the range 20–70° with Cu Kα (1.541 Å) radiation at a scan rate of 2° $min^{-1}$. Using AXIS ULTRA from AXIS 165, XPS (X-ray photoelectron spectroscopy) measurements was carried out by integrating with Kratos patented Magnetic immersion lens, spherical mirror analyzer and charge neutralization system. The morphology was studied using SEM, Hitachi—3000 and TEM (JEOL-ISM 2000). FT-IR studies were performed with a Spectrum-1000 (Perkin Elmer) spectrophotometer. UV–Visible absorption was recorded using shimadzu UV 2600 UV–Visible Spectrophotometer. Photoluminescence (PL) studies were carried out at room temperature using Horiba Fluorolog Spectrofluorimeter. The surface area was obtained by Brunner–Emmet–Teller (BET) method using Quanta chrome Nova-1000 surface analyzer under liquid nitrogen temperature.

Table 1 Chemical composition of Jatropha oil

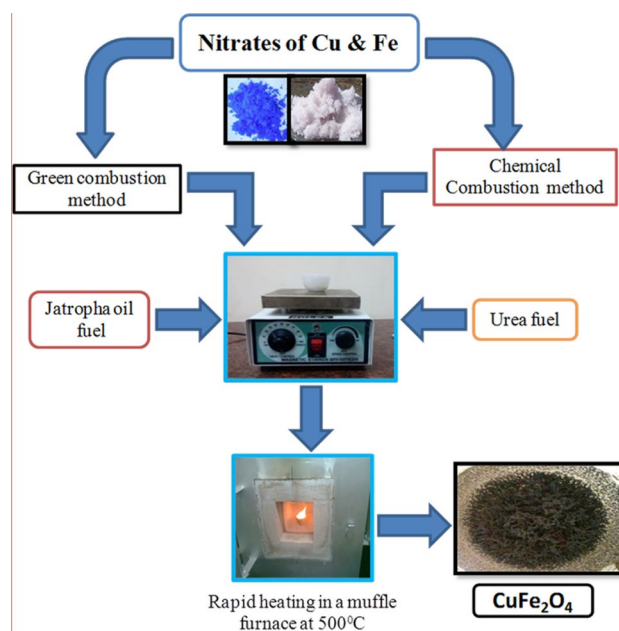| Parameters | Results |
|---|---|
| Color | Yellow colored liquid |
| Methyl esters of | |
| Caproic acid | Nil |
| Capryllic acid | Nil |
| Capric acid | Nil |
| Lauric acid | Nil |
| Myristic acid | Nil |
| Palmitic acid | 10.82% |
| Stearic acid | 7.14% |
| Oleic acid | 51.56% |
| Linoleic acid | 18.05% |
| Linolenic acid | 3.80% |
| Arachidonic acid | Nil |
| Behenic acid | 5.67% |
| Eruic acid | Nil |
| Lignoceric acid | Nil |



Fig. 1 Flow chart for the synthesis of CNPs by GCR & CCR
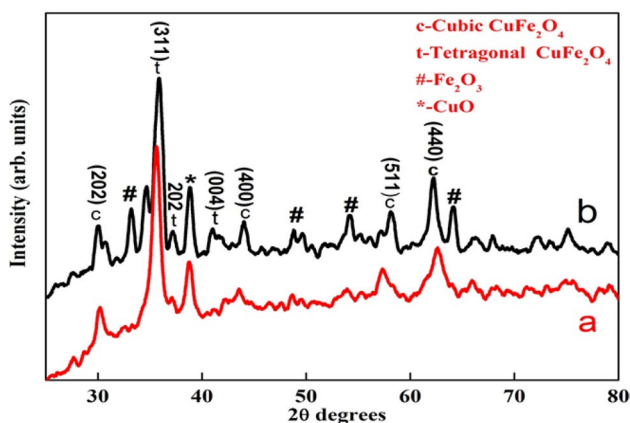
**Fig. 2** PXRD patterns of CNPs synthesized by **a** GCR, **b** CCR

## Photocatalytic activity measurements

The photocatalytic decomposition of dye was carried out under Sunlight for synthesized CNPs by degrading Malachite green (MG) dye. This reaction was conducted in between 11 am to 2 pm to avoid fluctuations in the intensity of sun rays. Here, 30 mg of prepared CNPs was treated with 250 ml of MG dye solution taken in a glass reactor. During the experiment, 5 ml of dye solution was pipetted out at regular intervals until complete decomposition of dye solution and finally adsorption was monitored using UV–Visible spectrophotometer. To check the endurance of synthesized CNPs, the experiment was repeated using same photocatalyst after washing and drying with fresh dye. The concentration of MG was analyzed by monitoring the absorbance at 618 nm.

## Results and discussion

### PXRD analysis

PXRD patterns of the synthesized CNPs were prepared by GCR and CCR routes as shown in the Fig. 2. PXRD pattern shows the major reflection peaks indexed as (202), (311),

(400), (004), (511) and (440) are well matched with JCPDS card No. 034-0425 having cubic and tetragonal spinel structures [24, 25]. The crystallization method proceeds along (311), (440) crystal planes and intensity of this planes was found to be maximum for GCR compared to CCR CNPs. Scherer's method was employed to observe the variation in crystallite size for prepared CNPs with different routes. The estimated results showed that the average crystallite size is ~ 8 and ~ 12 nm for $CNPs_4$ prepared by CCR and GCR, respectively and the details were given in Table 2.

### XPS analysis

To explain whether the Ferric (III) ions existed on the surface of CNPs (GCR), XPS spectra of was analyzed. Figure 3a shows the XPS spectrum in a wide energy range up to 1200 eV and $Cu_3s/Fe_3s/Cu_3p/Fe_3p$ and $O_2s$ core level regions are indicated in the figure by (#) and (+), respectively [26]. The Cu 2p line shows three pairs of lines at 935.38, 955.33 and 975.06 eV (Fig. 3b). Further, the investigated oxygen vacancies from the spectra O1s are asymmetric, indicating that multi-component oxygen species are present in the surface as shown in Fig. 3c. In the crystal structure, two terminal Fe–O groups perpendicular to the plane defined by four equatorial O atoms are present. The terminal Fe–O bonds of about 0.1 Å were shorter than the equatorial ones. These oxygen ions participating in two different bonds at 531.18 and 535.15 can be ascribed to the terminal and equatorial oxygen, respectively [27]. The Fe 2p spectra of the sample has four peaks centered at 711.49, 718.02, 724.04 and 742.5 eV can be assigned to $Fe^{3+}$ ion; no $Fe^{2+}$ peaks were observed (Fig. 3d). The extra lines present apart from Cu, Fe and O elements forming the compound are due to carbon impurities. A small quantity of carbon in the results was mainly attributed to the adventitious hydrocarbon from XPS itself (Fig. 3e).

### Morphological studies

SEM micrographs of CNPs are prepared by GCR and CCR methods at different magnification as shown in the Fig. 4. In the combustion method, the temperature is uniformly

**Table 2** The estimated crystalte parameters of $CuFe_2O_4$ nanoparticles

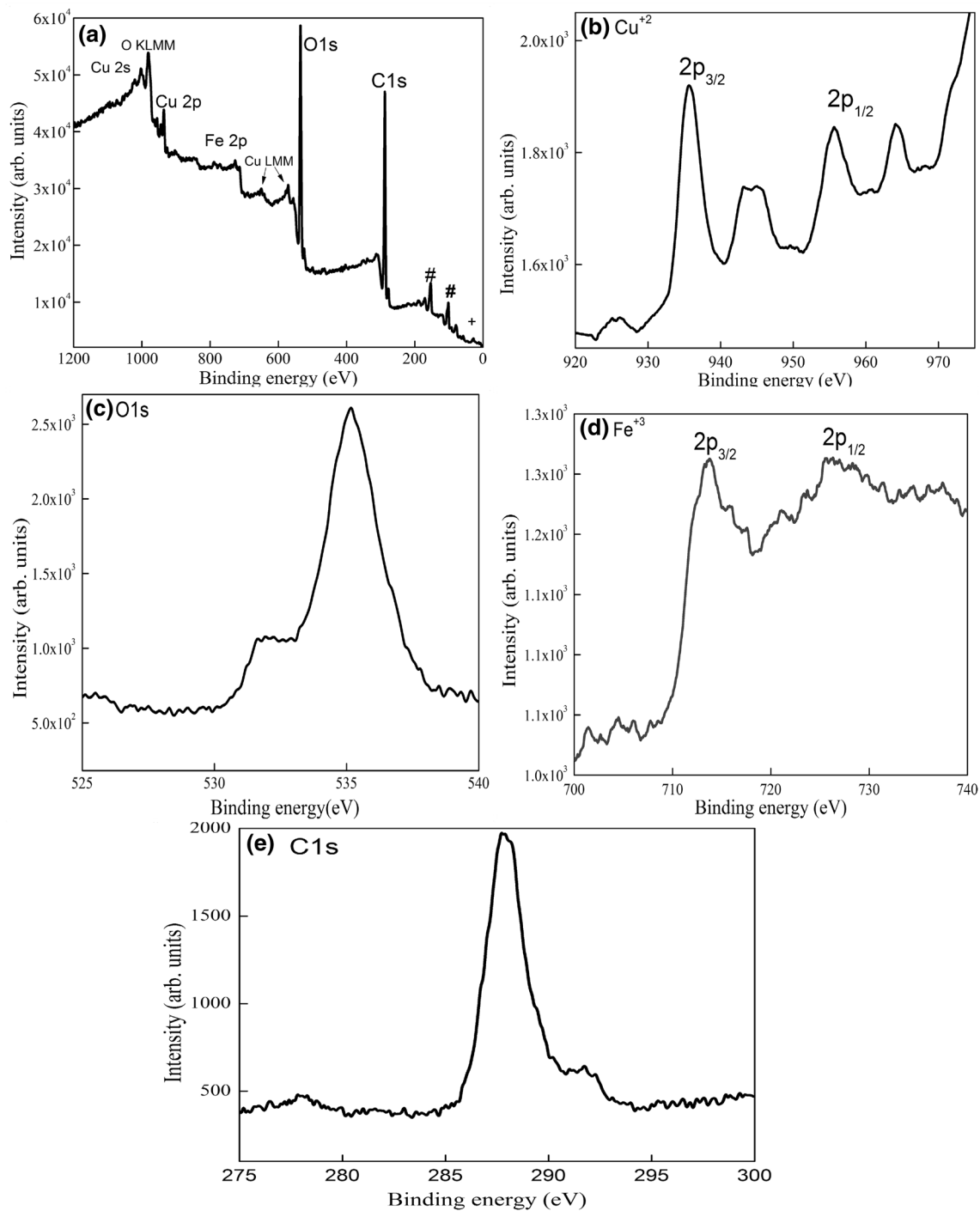| hkl | $D = \frac{0.9\lambda}{\beta \cos\theta}(nm)$ | $d = \frac{\lambda}{2\sin\theta}10^{-10}m$ | $\delta = \frac{1}{D^2}10^{-03}$ | $SF = \frac{2\pi^2}{45\,(3\tan\theta)^{1/2}}$ |
|---|---|---|---|---|
| 311 (GCR) Tetragonal | 10.6 | 2.516 | 8.899 | 0.4469 |
| 311 (CCR) Tetragonal | 9.0 | 2.6640 | 12.790 | 0.4466 |
| 440 (GCR) Cubic | 14 | 1.2541 | 5.1757 | 0.2826 |
| 440 (CCR) Cubic | 10.4 | 0.9765 | 9.2455 | 0.2178 |

**Fig. 3** XPS spectra of CNPs **a** survey spectrum, **b** Cu $^{2+}$, **c** O 1 s, **d** Fe$^{3+}$, **e** C 1 s peaks

distributed and transferred to the interior of the sample, which made the evolution of gases and release of enormous amount of heat to form spinel ferrites [28]. This typical porous network was commonly observed in combustion synthesis. There will be simultaneous formation of pores and also small particles near the pores due to the escape of gas with high pressure.

The formation process of cubic and tetragonal structure with pores was predicted as represented in Fig. 5. When ferric nitrate was mixed with copper ferrite in the presence of jatropha oil extract, the $Cu^{2+}$ and $Fe^{2+}$ ions distribute uniformly and form a complex structure with active fatty acids such as oleic acid. After, the complex structure reacts with proteins at a low temperature to form superstructure. When
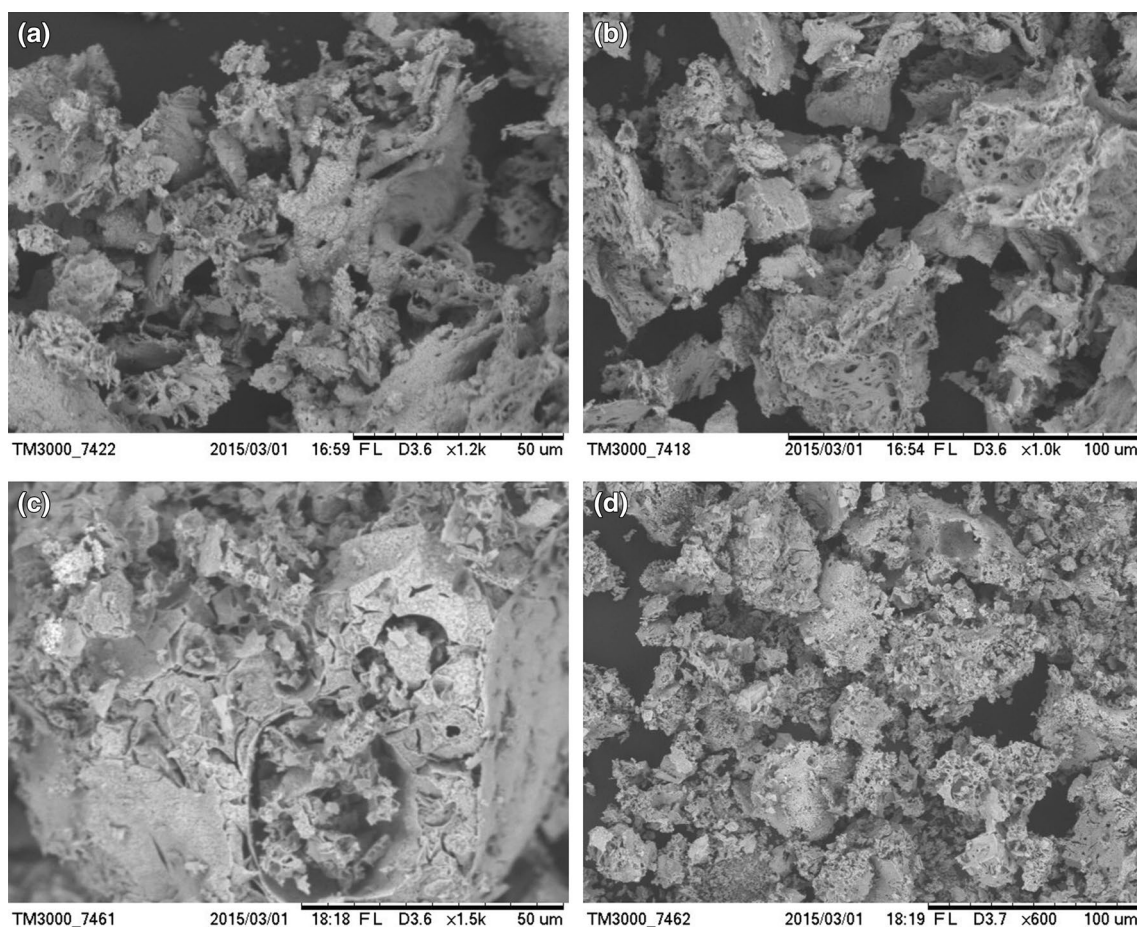
**Fig. 4** SEM images of CNPs synthesized by GCR (**a**, **b**) and CCR (**c**, **d**) at different magnification

subjected to heat treatment, this network undergoes slow decomposition. In summary, fatty acid molecules that interact with divalent $Cu^{2+}$ cations forming bridges between two hydroxyl groups from two different chains comes in close contact. This polymeric binding was responsible for the conjugation of all these families of compounds present in the oil extract and expected to get different structure. The formation process of cubic and tetragonal structure involves the steps of complex reaction to form morphologies as explained in SEM.

Figure 6 shows the TEM image of CNPs synthesized by GCR. The TEM image consists of large number of agglomerated NPs (Fig. 6a, b) [29]. Further, HRTEM image clearly resolved interplanar distance and lattice fringes separated by a distance of 0.3 nm corresponding to the (311) crystal plane of tetragonal phase (Fig. 6c, d). The clear rings observed in SAED pattern (Fig. 6e) confirm the polycrystalline nature of the prepared samples.

## FTIR studies

To confirm the phase transformation and purity of the CNPs prepared by GCR and CCR method, the FTIR spectra were recorded in the range 400–4000 $cm^{-1}$ (Fig. 7). The bands in the range 400–600 $cm^{-1}$ were due to vibrations of metal ions. The two prominent absorption bands of metal–oxygen bond corresponding to the vibration of tetrahedral and octahedral complexes were observed at ~ 523.4 and ~ 415.5 $cm^{-1}$, respectively. Further, the bond observed at ~ 523.4 $cm^{-1}$ was attributed to the stretching vibration of tetrahedral group Cu–O and the bond observed at ~ 415.5 $cm^{-1}$ was attributed to the octahedral complex Fe–O vibrations [30]. Both the samples showed wide band at 3421 $cm^{-1}$ which indicates the presence of hydroxyl groups and band observed at ~ 1651 $cm^{-1}$ was attributed to the O–H bending vibration of adsorbed water molecules [31].
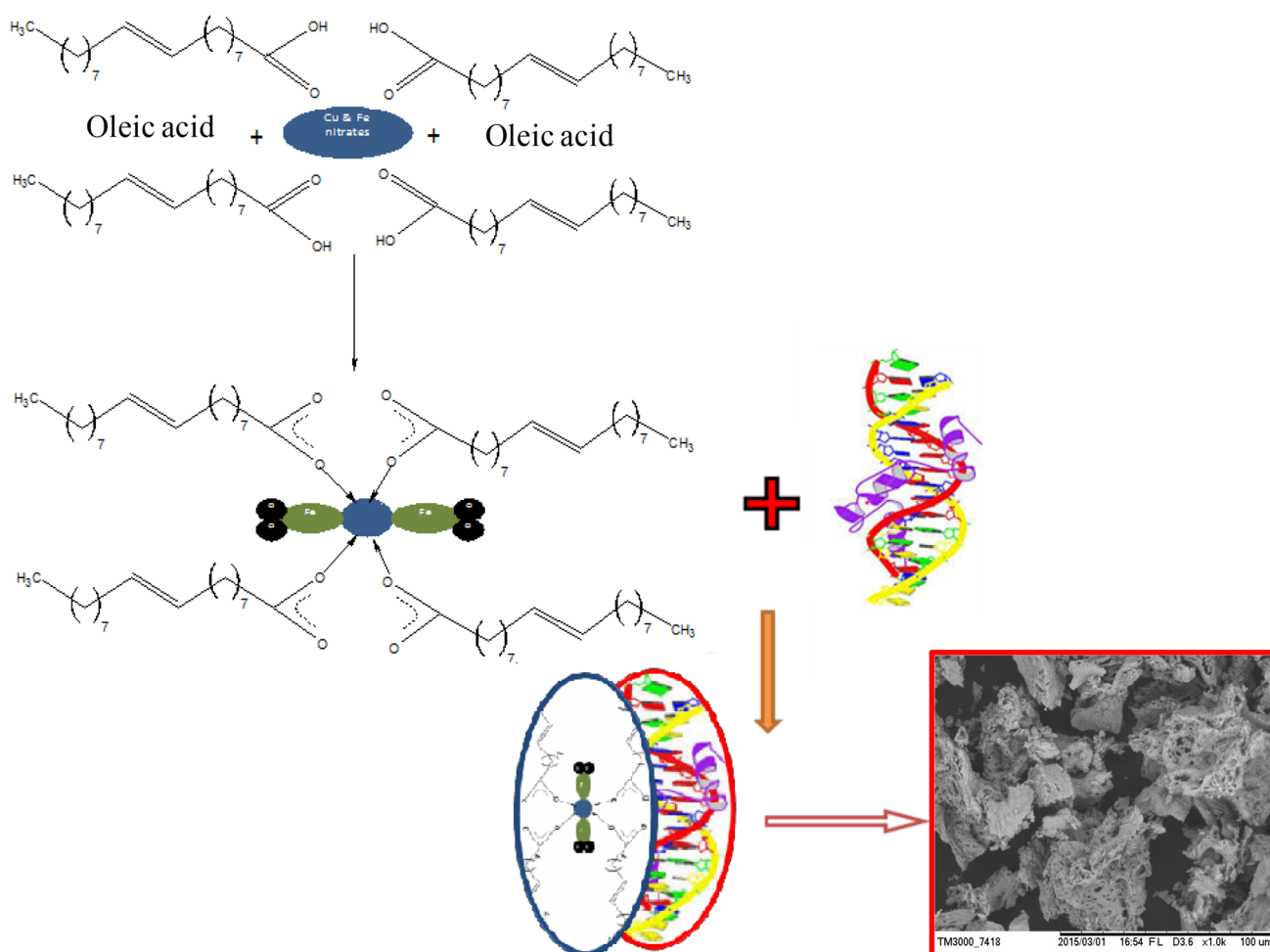
**Fig. 5** Probable Mechanism for formation of CNPs by GCR

## Electrochemical studies

Cyclic Voltammetry (CV) was useful to study the electrochemical characteristics and supercapacitive nature of the CNPs synthesized by GCR and CCR modified with carbon paste electrode. The CV experiments were carried out with conventional three electrode system in 0.1 M KNO$_3$ electrolyte in the potential window 1.2 to − 1.2 V at the range of scan rate of 50 mV/s and the results are revealed in the Fig. 8. It is noteworthy that the GCR CNPs synthesized by green combustion-modified electrode possess redox peak with enhanced peak current compared to CCR CNPs can be ascribed to its good photocatalytic activity. From the above explanation, it is clear that the capacitances of the samples follow the order: GCR CNPs > CCR CNPs.

Figure 9 shows typical EIS Nyquist plots of the CNPs prepared by GCR & CCR. The Nyquist plot of the electrodes displays a single semicircle at the high-frequency region and a line at the low-frequency region, indicating the electrochemical reaction at the electrodes is controlled by a mixed process of charge transfer and diffusion. Further, the arc radius of the EIS spectra reflects the interface layer resistance arising outside the electrode. Smaller the arc radius indicates that higher charge transfer effectiveness [32]. The arc radius for GCR and CCR-synthesized CNPs was found to be 31 and 48 Ω, respectively. The smaller charge transfer resistance provides more contribution for enhanced photocatalytic activity by easy transfer of charge. Thus, GCR CNPs have smaller arc radius with enhanced photocatalytic activity.

The impedance curve can be explained by an equivalent Randles circuit that contains solution resistance ($R_s$), double layer capacitance ($C_{dl}$), charge transfer resistance ($R_{ct}$), and Warburg impedance. The equivalent circuit for CNPs synthesized by GCR and CCR are shown in inset of Fig. 9. At higher frequency region, only resistive effect is present whereas lower frequency region comprises capacitive and resistive effect. The circuit consists of resistance and capacitance in parallel contributing to acquire a semicircle at higher frequency region in

**Fig. 6** TEM (**a–c**), HRTEM (**d**) and SAED pattern (**e**) of CNPs (GCR)
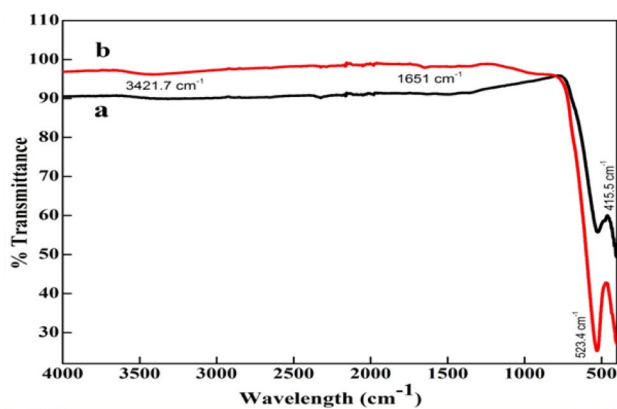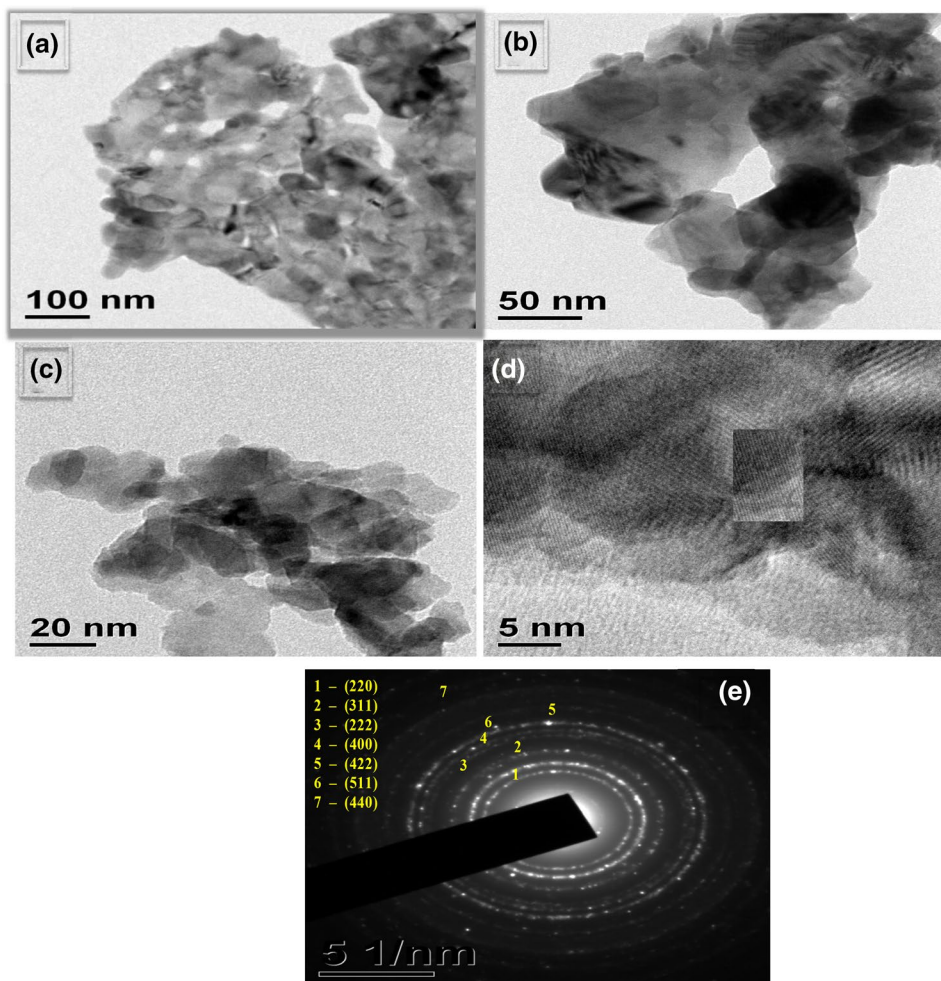


**Fig. 7** FTIR spectra of synthesized CNPs by **a** GCR & **b** CCR

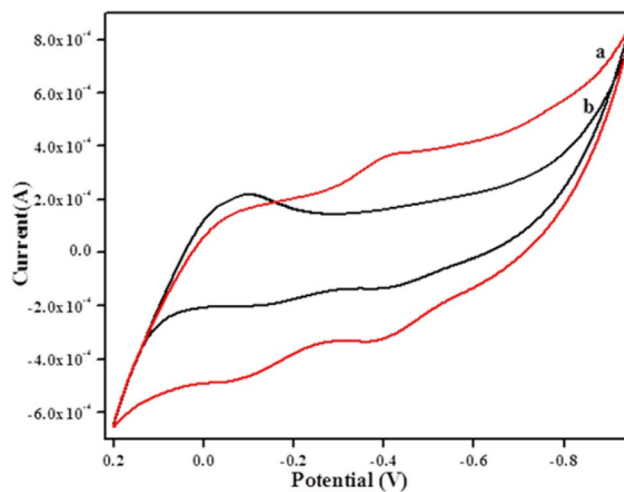Nyquist plot whereas Warburg impedance contributes to slant in the line at lower frequency region.

**Fig. 8** CV plots for CNPs synthesized by GCR (**a**) & CCR (**b**) at potential range 1.2 to − 1.2 V with scan rate 50 mV/s
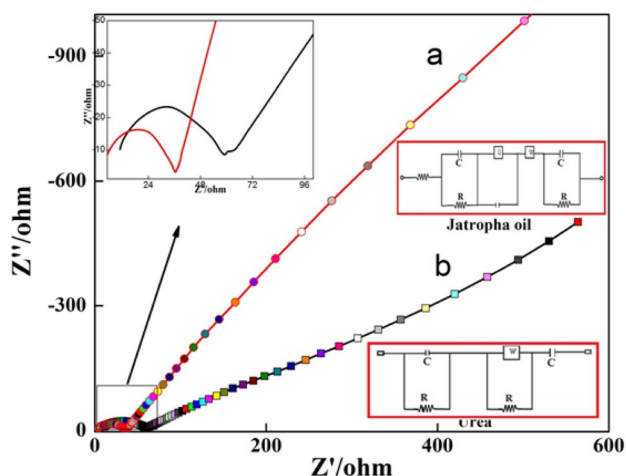
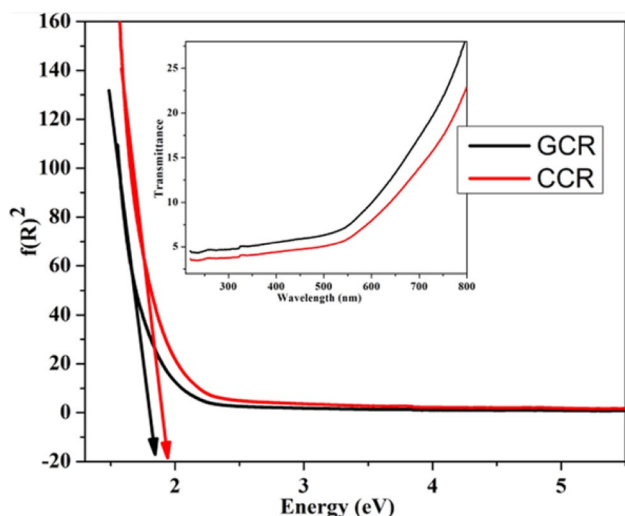**Fig. 9** Impedance plot of CNPs synthesized by (**a**) GCR & (**b**) CCR (Inset: Circuit fitting program for CNPs)



**Fig. 10** Wood and Tauc's plot to find bandgap and the variation of bandgap of CNPs by **a** GCR & **b** CCR (**b**) (Inset: Transmittance vs wavelength of CNPs (GCR & CCR))

## Diffuse reflectance spectral (DRS) analysis

Figure 10 shows the DRS of CNPs to find energy bandgap for GCR and CCR prepared CNPs. The spectra are plotted in terms of $F(R)^n$ in $Y$-axis and energy in $X$-axis. Kubelka–Munk equation [33] at any wavelength is represented as follows:

$$F(R) = \frac{(1-R)^2}{2R}, \tag{1}$$

where $R$ the absolute reflectance of the sample and $F(R)$ is Kubelka–Munk function. The optical band gap represents

the electron excitation from the valance band to conduction which is determined by the following relation.

$$(F(R)h\upsilon)^n = A(h\upsilon - E_g), \tag{2}$$

where $n = 2$ for a direct allowed transition, $n = 1/2$ for an indirect allowed transition, A is the constant and $h\upsilon$ is the photon energy. To get the direct bandgap, the linear part of the curve was extrapolated to $(F(R)\,h\upsilon)^2 = 0$. The bandgap energy ($E_g$) values are estimated from the plot and found to be 1.96 and 1.84 eV for CCR and GCR CNPs, respectively. The expected changes in the band gap values in CNPs are due to the increase of carrier concentrations which lead to the Burstein–Moss effect [34].

## Photoluminescence (PL) studies

PL spectra were useful to analyze the luminescence properties and the information regarding the recombination of photoexcited charge carriers, it is a useful technique to understand the recombination nature of electron–hole pairs in semiconductor particles. Figure 11a depicts the excitation spectra of CNPs by monitoring the emission line at 425 nm. Figure 11b, c represents the emission spectra of CNPs samples excited under 313 and 323 nm, respectively, at room temperature. The PL intensity of the samples excited at 313 nm is stronger than that under 323 nm indicating that an efficient energy transfer. The peak at 421 nm indicates the radiative defect related to the interface traps that exist at the grain boundary corresponds to the blue emission [35, 36]. The peak at 532 nm corresponds to green emission due to the singly ionized oxygen vacancy and deep level or trap state emission. GCR prepared CNPs showed stronger PL emission peak and hence the method of preparation also plays a very important role. Therefore, oxygen vacancies and defects present in the GCR sample will bind the photo-induced electrons easily to form excitons indicating increase in PL intensity. PL emission properties of these CNPs can be controlled by methodology signifying their enhanced capabilities in photoluminescent and photocatalytic properties.

The Commission International De I-Eclairage (CIE) 1931chromaticity coordinates for CNPs prepared by GCR and CCR for the luminous color was studied by PL spectra. The CIE coordinates of the CNPs lies well within the blue region as represented in Fig. 12a. Hence, the present phosphor might be a potential candidate for display applications. Correlated color temperature (CCT) estimated using CIE coordinates and CCT value of CNPs (Fig. 12b) was found to be 252,119 and 259,556 K, respectively, for GCR and CCR, which indicate the warm white light used for home appliances [37].
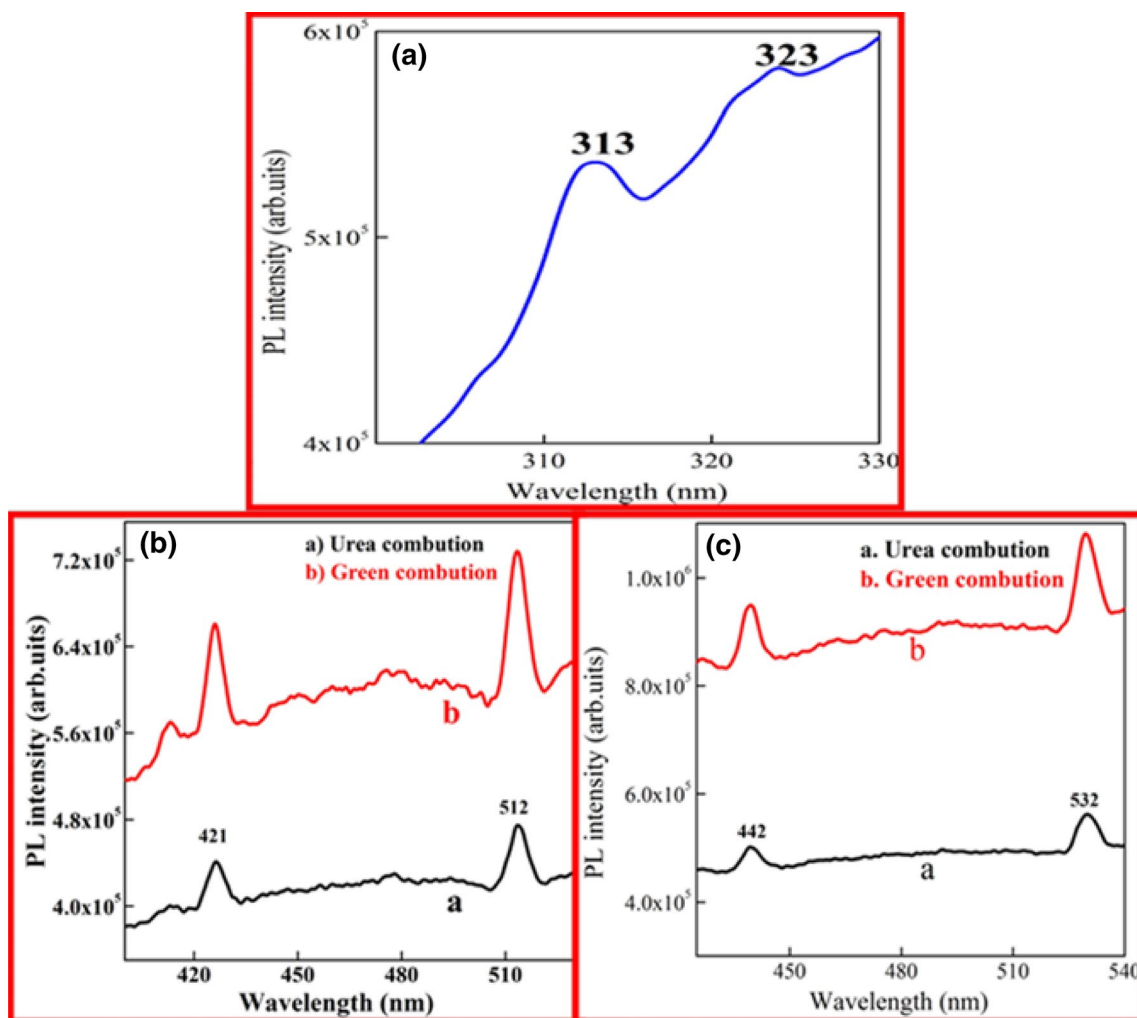
**Fig. 11** **a** PL excitation spectrum of CNPs, **b** PL emission spectrum of CNPs excited at 313 nm, **c** PL emission spectrum of CNPs excited at 313 nm. [GCR (**a**) & CCR (**b**)]

## BET analysis

Braunauer, Emmett and Teller (BET) analysis was used to study the porosity and textural properties of the synthesized CNPs by GCR CCR. The combustion-derived products usually have a large surface area due to liberation of heat (exothermicity). The BET surface area of CNPs was found to be 13.51 $m^2$/g (GCR) and 11 $m^2$/g (CCR), respectively, as shown in Fig. 13. The large surface area of formed sample is due to uniform distribution of nanosized particle as observed in SEM images and the same may be supported by Scherrer's formula in XRD. Average pore diameter of the sample is found to be 150.66 Å for CNPs (GCR) and 84.74 Å for CNPs (CCR), respectively, and it confirms that the prepared samples are mesoporous. Inset of Fig. 13 shows the average pore diameter and isotherms for GCR and CCR CNPs, respectively. It is clear that all isotherm curves reach a plateau when the relative pressure

reaches unity [38]. This indicates that the materials prepared have no pores in macropore region (i.e., 500 Å), means pores are in mesopore region and the sample is mesoporous.

## Photocatalytic activity

In the present study, the photocatalytic decomposition of MG dye was carried out for CNPs prepared by GCR and CCR routes. CNPs (GCR) photocatalyst displays the best performance due to the uniform structure less particle size, increase in the amount of dispersion of particles per volume, increase in number of active sites compared to other sample. Hence the particle size also plays an important role in the catalytic activity [39, 40]. It was found that the photodecolorization of MG for CNPs (GCR) was 96%, whereas it was only 83% for CNPs (CCR) (Fig. 14a, b).
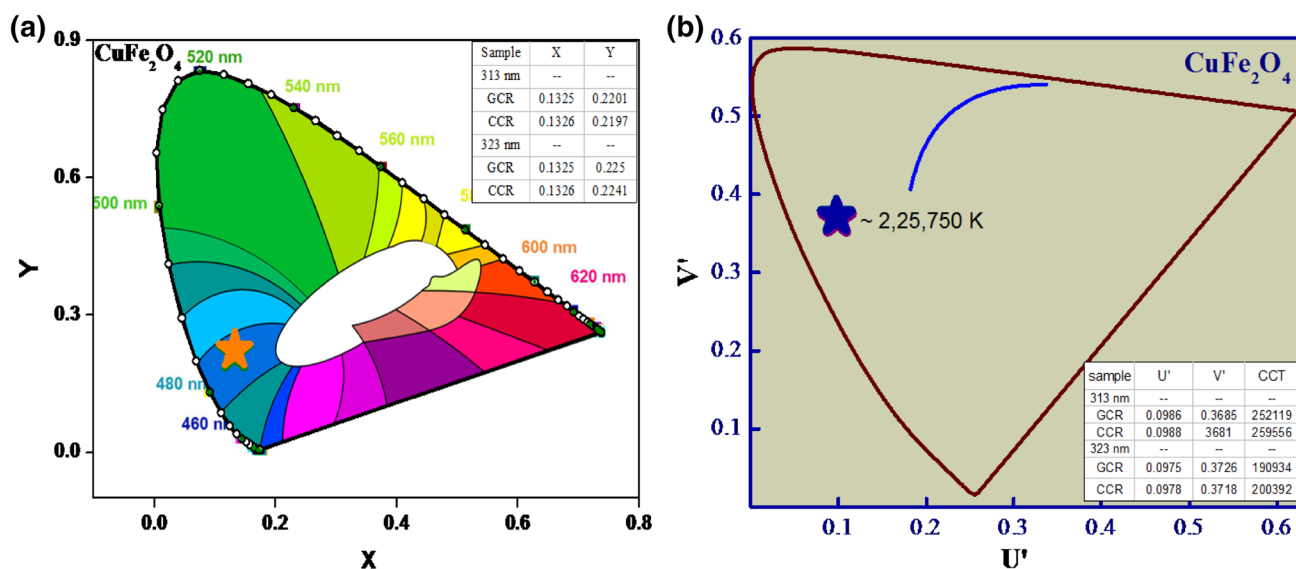
**Fig. 12** **a** CIE chromaticity diagram of CNPs synthesized by GCR and CCR (Inset: CIE chromaticity coordinates), **b** CCT diagram of CNPs synthesized by GCR and CCR (Inset: Color correlated temperature values)

## Mechanism of Photocatalytic activity

The mechanism occurs in the photocatalytic activity of MG dye under UV and sunlight was shown in Fig. 14c & 14d. On the surface of the photocatalyst, oxygen molecules ($O_2$) and water molecules ($H_2O$) are absorbed easily owing to the porous spinel structures under UV light irradiation. These molecules are not only adsorbed on outer surface but also adsorbed on the internal surface of CNPs. This photocatalyst was dispersed in MG dye solution and kept under sunlight irradiation. Also, CNPs (Fig. 14d) get adsorbed on inner as well as outer surface of spinel porous structure, and captures the incident light to some extent in the interior of the spinel



**Fig. 13** Nitrogen adsorption and desorption isotherms and pore volume distribution curve (inset) of (CNPs synthesized by **a** GCR & **b** CCR)

structure due to the multi reflection effect. As mentioned, porous structure is mainly responsible for the absorption of aforementioned molecules and capture of incident light. Chemical bonds in the MG molecules will be broken down under irradiation and jump to excited state or can be directly self-disintegrated. On the other hand, when CNPs absorb photons with sufficient energy, these electrons (e −) jump into the conduction band (CB) from the valence band (VB), leaving behind the same number of holes (h +) in the VB. If these photogenerated electrons and holes become free, they automatically move towards the surface of the CNPs and are got captured by absorbed $O_2$, $OH^-$. Of course, the absorbed MG molecules can also capture the carriers to ionize it. After that, a lot of superoxide radicals ($O^{2\bullet-}$) and hydroxyl radicals ($OH^\bullet$) are formed. These produced active radicals react with the ionized MG molecules to decompose them into the harmless $H_2O$, $CO_2$, and mineral acids ($NO^{2-}$, $NO^{3-}$, or $SO4^{2-}$) [37, 41–44]; during this step, partial strong oxidizing holes (h +) can also directly participate in the decomposition of the MG molecules. According to the results obtained, the self decomposition of MG molecules is very negligible.
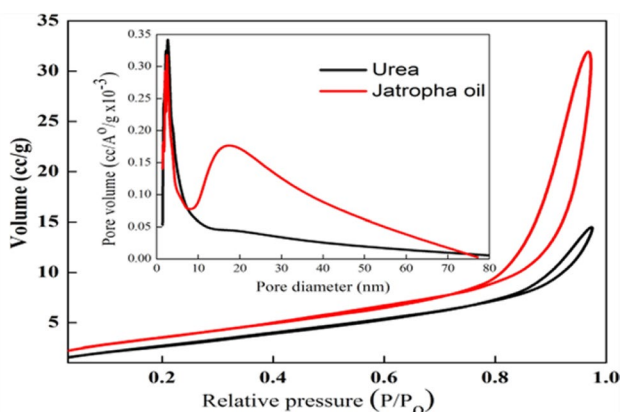
## Kinetic studies

The decomposition process of MG shows the first-order kinetic model, which is generally suited since the initial concentration of the pollutant is low and its kinetics can be expressed as $\ln(C/C_0) = -kt$. Where $k$ is the apparent reaction rate constant, $C_0$ is the initial concentration of aqueous MG, t is the reaction time, and C is the concentration
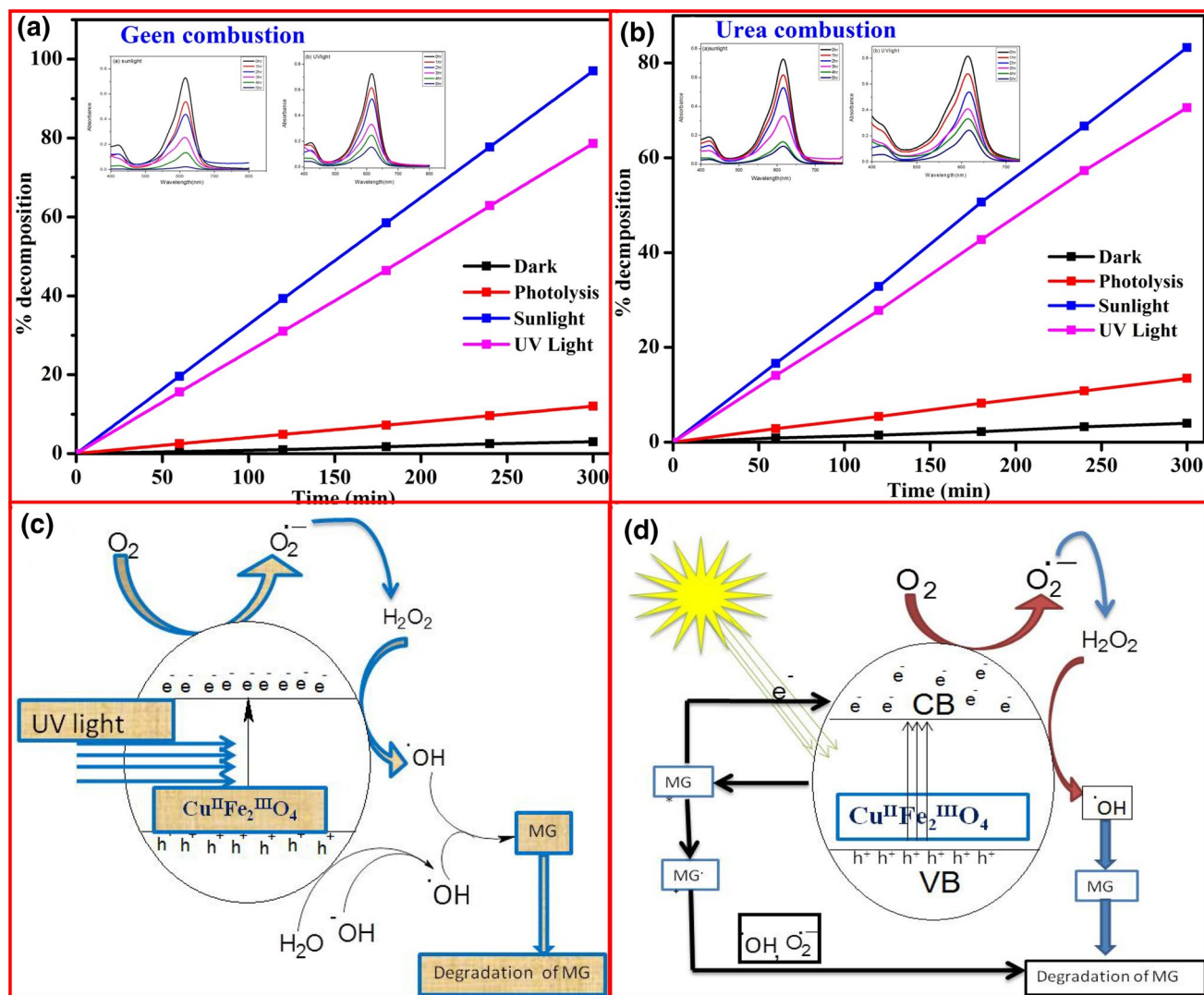
**Fig. 14** **a** % Decomposition of MG under UV light and sunlight irradiation for CNPs synthesized by GCR (Inset: Spectral absorbance of MG with the variation of irradiation time under UV and Sunlight irradiation). **b** % Decomposition of MG under UV light and sunlight irradiation for CNPs synthesized by CCR (Inset: Spectral absorbance of MG with the variation of irradiation time under UV and sunlight irradiation). **c** Mechanism for the photocatalytic decomposition of MB under UV light irradiation **(d)** Mechanism for the photocatalytic decomposition of MB under sunlight irradiation

of aqueous MG at the reaction time *t*. Figure 15a represents first-order plots for decomposition of MG for GCR-synthesized CNPs under sunlight and UV light irradiation. The reaction rate constants determined were found to be $10.61 \times 10^{-3}$ and $5.203 \times 10^{-3}$ min$^{-1}$ for sunlight and UV light, respectively. Figure 15b displays the first-order plots for the decomposition of MG for CCR-synthesized CNPs under sunlight and UV light irradiation. The reaction rate constants calculated were $6.445 \times 10^{-3}$ and $4.085 \times 10^{-3}$ min$^{-1}$ for sunlight and UV light, respectively.

4-Chlorophenol (4-CP) is a common chemical that is used extensively in a variety of industrial applications. Therefore, it is also chosen as a model pollutant in this work. Figure 15c shows the decomposition rate of 4-CP on effective

GCR-derived CNPs under UV and sunlight irradiation. It can be seen that decomposition of 4-CP was almost consistent with decomposition of MG dye for GCR CNPs under UV and sunlight.

The CNPs were subjected to five cyclic runs to assess the stability of the photocatalyst as shown in Fig. 15d. The GCR CNPs were separated using a magnet and washed repeatedly with water and finally dried. To the fresh dye solution in the photocatalytic reactor, dried photocatalyst was added and the decomposition was carried out. The decomposition percentage was same until four cycles after which slight decrease is observed due to the sample loss during washing. Hence, the photocatalyst was found to be stable even after five cyclic runs.
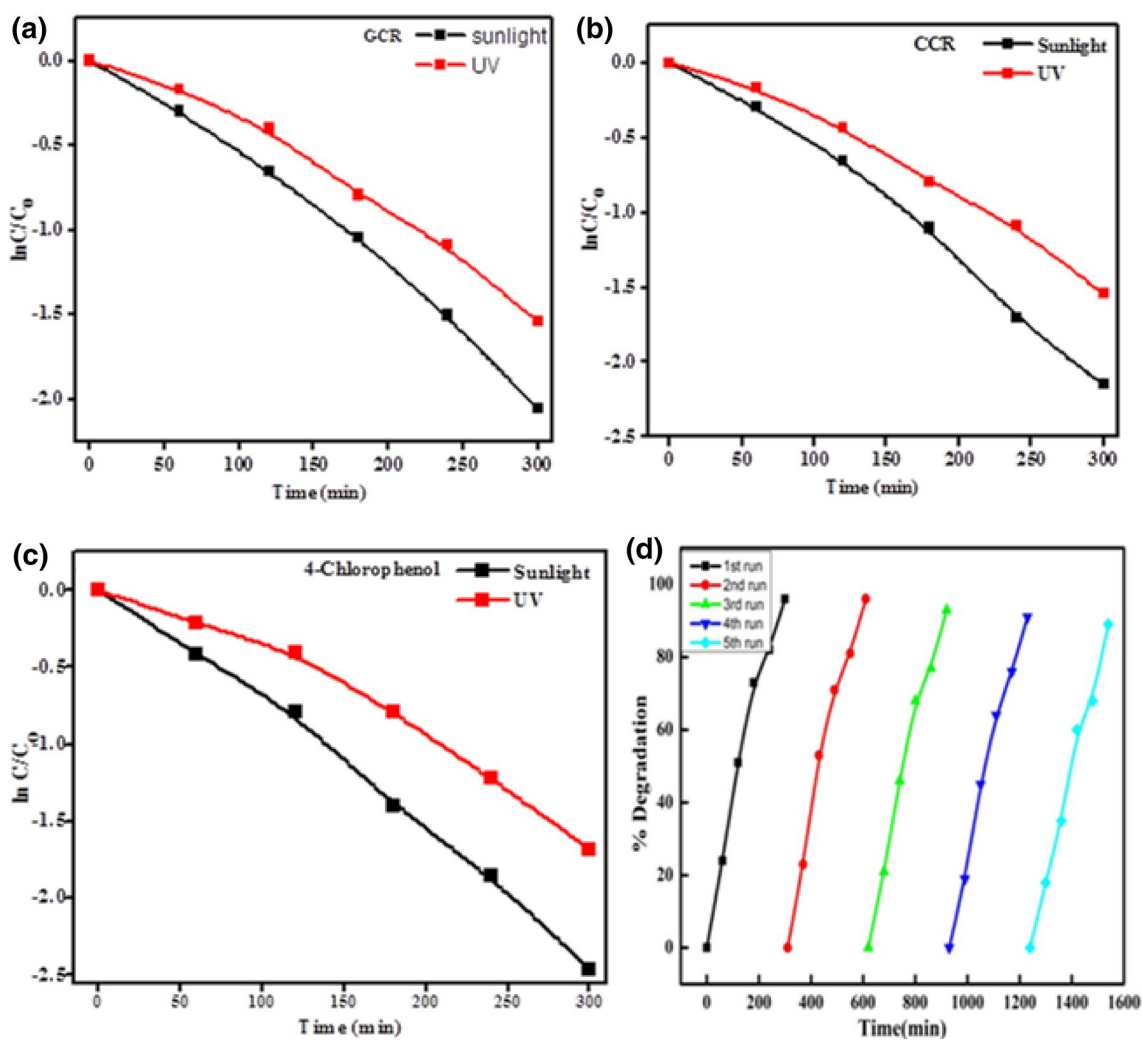
**Fig. 15** **a** Plot of ln ($C/C_0$) versus irradiation time for the decomposition of MG under UV and sunlight irradiation for CNPs (GCR). **b** Plot of ln ($C/C_0$) versus irradiation time for the decomposition of MG under UV and sunlight irradiation for CNPs (CCR). **c** Plot of ln ($C/$ $C_0$) versus irradiation time for the decomposition of 4-chlorophenol under UV and sunlight irradiation. **d** Reusability of the CNPs synthesized by GCR for five consecutive recycle runs

## Conclusions

The present work demonstrated the efficient ability of CNPs prepared by GCR and CCR for structural, photoluminescence and photocatalytic properties. PXRD pattern and TEM analysis clearly confirms the formation of cubic and tetragonal phase. The broadness of the excitation spectrum indicates the possibility of using CNPs as UV LED chips. CNPs prepared by CCR and GCR exhibits blue emission with average of 225,750 K CCT value. Thus, the present CNPs can serve as a potential candidate for light emitting diodes. It was found that CNPs (GCR) is highly active towards the photo-decolorization of MG with very high yield (96%), because of the smaller particle size, higher surface defects and the presence of more number of active sites. Further, it should be pointed out that the $CuFe_2O_4$ photocatalysts are recoverable and recyclable that exhibit high photocatalytic efficiency to decolorize MG dye. It was evident from the above results that the eco-friendly green combustion route was found to be efficient compared to chemical combustion route.

## Compliance with ethical standards

**Conflict of interest** All authors declare that they have no conflict of interest.

**Open Access** This article is distributed under the terms of the Creative Commons Attribution 4.0 International License (http://creativecommons.org/licenses/by/4.0/), which permits unrestricted use, distribution, and reproduction in any medium, provided you give appropriate credit to the original author(s) and the source, provide a link to the Creative Commons license, and indicate if changes were made.

## References

1. Nafisa Ali, A.K.: Kurchania and Swati Babel Bio-methanisation of Jatropha curcas defatted waste. J. Eng. Technol. Res. **2**, 038–043 (2010)
2. Ahmed, Fahad, Giwa, S.O., Ibrahim, M., Giwa, A.: Production of biodiesel from *Jatropha Curcas* seed oil using base catalysed transesterification. Int. J. Chem. Tech. Res. **9**, 322–332 (2016)
3. Surendra, B.S., Veerabhadraswamy, M.: Microwave assisted synthesis of polymer via bioplatform chemical intermediate derived from Jatropha deoiled seed cake. J. Sci. **2**, 340–346 (2017)
4. Francis, George, Oliver, John, Sujatha, Mulpuri: Non-toxic jatropha plants as a potential multipurpose multi-use oilseed crop. Ind. Crops Prod. **42**, 397–401 (2013)
5. Surendra, B.S., Veerabhadraswamy, M.: Microwave assisted synthesis of Schiff base via bioplatform chemical intermediate (HMF) derived from Jatropha deoiled seed cake catalyzed by modified Bentonite clay. J. Mater. Today: Proc. **4**, 11727–11736 (2017)
6. Mitoraj, D., Kisch, H.: The nature of nitrogen-modified titanium dioxide photocatalysts active in visible light. Angew. Chem. Int. Ed. Engl. **47**, 9975–9978 (2008)
7. Xu, X., Liu, G., Randorn, C., Irvine, J.T.S.: g-C3N4 coated SrTiO3 as an efficient photocatalyst for H2 production in aqueous solution under visible light irradiation. Int. J. Hydrogen Energy **36**, 13501–13507 (2011)
8. Fu, Y., Chen, Q., He, M., Wan, Y., Sun, X., Xia, H., Wang, X.: A multifunctional heteroarchitecture for photocatalysis and energy storage. Ind. Eng. Chem. Res. **51**, 11700–11709 (2012)
9. Shu, X., He, J., Chen, D.: Visible-light-induced photocatalyst based on nickel titanate nanoparticles. Ind. Eng. Chem. Res. **47**, 4750–4753 (2010)
10. Guo, R.Q., Fang, L.A., Dong, W., Zheng, F.G., Shen, M.R.: Enhanced photocatalytic activity and ferromagnetism in Gd doped BiFeO3 nanoparticles. J. Phys. Chem. C **114**, 21390–21396 (2010)
11. Al-Ghouti, M.A., Khraisheh, M.A., Allen, S.J., Ahmad, M.N.: The removal of dyes from textile wastewater: a study of the physical characteristics and adsorption mechanisms of diatomaceous earth. J. Environ. Manag. **69**, 229–238 (2003)
12. Borse, P.H., Hwichan, J., Choi, S.H., Hong, S.J., Lee, J.S.: Phase and photoelectrochemical behavior of solution-processed $Fe_2O_3$ nanocrystals for oxidation of water under solar light. Appl. Phys. Lett. **93**, 173103 (2008)
13. Tamaura, Y., Ueda, Y., Matsunami, J., Hasegawa, N., Nezuka, M., Sano, T., Tsuji, M.: Solar hydrogen production by using ferrites. Sol. Energy **65**, 55–57 (1999)
14. Han, S.B., Kang, T.B., Joo, O.S., Jung, K.D.: Water splitting for hydrogen production with ferrites. Sol. Energy **81**, 623–628 (2007)
15. Yu, S.H., Yoshimura, M.: Ferrite/metal composites fabricated by soft solution processing. Adv. Funct. Mater. **12**, 9–15 (2002)
16. Nan, C.W., Bichurin, M.I., Dong, S., Viehland, D., Srinivasan, G.: Multiferroicmagnetoelectric composites: Historical perspective, status, and future directions. J. Appl. Phys. **103**, 031101 (2008)
17. Jang, J.S., Hong, S.J., Lee, J.S., Borse, P.H., Kim, H.G.: Synthesis of zinc ferrite and its Photocatalytic applications under sun light. J. Korean Phys. Soc. **54**, 204–208 (2009)
18. Dom, R., Subasri, R., Radha, K., Borse, P.H.: Synthesis of solar active nano crystalline ferrite, MFe2O4 (M: Ca, Zn, Mg) photocatalyst by microwave irradiation. Solid State Commun. **151**, 470–473 (2011)
19. Jacob, B.P., Kumar, A.: Pant RP Singh S, Mohammed EM, Influence of preparation method on structural and magnetic properties of Nickel ferrite nanoparticles. Bull. Mater. Sci. **34**, 1345–1350 (2011)
20. Cho, S., Jung, S.H., Lee, K.H.: Morphology-controlled growth of ZnO nanostructures using microwave irradiation: from basic to complex structures. J. Phys. Chem. C **112**, 12769–12776 (2008)
21. Kumar, E.R., Jayaprakash, R., Devi, G.S., Reddy, P.S.: Synthesis of Mn substituted CuFe2O4nanoparticles for liquefied petroleum gas sensor applications. Sens Actuators B **191**, 186–191 (2014)
22. RanjithKumar, E., Jayaprakash, R., SaralaDevi, G., Siva, P.: Prasada Reddy Magnetic, dielectric and sensing properties of manganese substituted copper ferrite nanoparticles. J. Magn. Magn. Mater. **355**, 87–92 (2014)
23. Banat, F., Pal, P., Jwaied, N., Al-Rabadi, A.: Extraction of olive oil from olive cake using soxhlet apparatus. Am. J. Oil Chem. Technol. **1**, 2326–6570 (2013)
24. Sarode, Sachin A., Bhojane, Jeevan M., Nagarkar, Jayashree M.: An efficient magnetic copper ferrite nanoparticle: for one pot synthesis of 2-substituted benzoxazole via redox reactions. Tetrahedron Lett. **56**, 206–210 (2015)
25. Vidya, Y.S., Gurushantha, K., Nagabhushana, H., Sharma, S.C., Anantharaju, K.S., Shivaku-mara, C., Suresh, D., Nagaswarupa, H.P., Prashantha, S.C., Anilkumar, M.R.: Phase transformation of $ZrO_2$:$Tb^{3+}$ nanophosphor: Color tunable photoluminescence and photocatalytic activities. J. Alloy Compd. **622**, 86–96 (2015)
26. Rashad, M.M., Mohamed, R.M., Ibrahim, M.A., Ismail, L.F.M., Abdel-Aal, E.A.: Magnetic and catalytic properties of cubic copper ferrite nanopowders synthesized from secondary resources. Adv. Powder Technol. **23**, 315–323 (2012)
27. Liu, Tian, Wang, Linsheng, Yang, Ping: Bingyuan Hu T, Preparation of nanometer CuFe2O4 by auto-combustion and its catalytic activity on the thermal decomposition of ammonium perchlorate. Mater. Lett. **62**, 4056–4058 (2008)
28. Selvan, R.K.: Augustin CO, LJ Berchmanns, R Saraswathi. Combustion synthesis of $CuFe_2O_4$. Mater. Res. Bull **38**, 41–54 (2003)
29. Prasad, B.D., Nagabhushana, H., Thyagarajan, K., Nagabhushana, B.M., Jnaneshwara, D.M., Sharma, S.C., Shivakumara, C., Gopal, N.O., Ke, S.-C., Chakradhar, R.P.S.: Magnetic and dielectric interactions in nano zinc ferrite powder: prepared by self-sustainable propellant chemistry technique. J. Magnt Magn Mater. **358**, 132–141 (2014)
30. Jnaneshwara, D.M., Avadhani, D.N., Prasad, B.D., Nagabhushana, H., Nagabhushana, B.M., Sharma, S.C., Prashantha, S.C., Shivakumara, C.: Role of $Cu^{2+}$ ions substitution in magnetic and conductivity behavior of nano-$CoFe_2O_4$. Spectrochim. Acta Part A Mol. Biomol. Spectrosc. **132**, 256–262 (2014)
31. Jnaneshwara, D.M., Avadhani, D.N., Daruka, Prasad B., Nagabhushana, B.M., Nagabhushana, H., Sharma, S.C., Prashantha, S.C., Shivakumara, C.: Effect of zinc substitution on the nanocobalt ferrite powders for nanoelectronic devices. J. Alloys Compd **587**, 50–58 (2014)

32. Ansari, S.A., Khan, M.M., Kalathil, S., Nisar, A., Lee, J., Cho, M.H.: Band gap narrowing of titanium dioxide (TiO$_2$) nanocrystals by electrochemically active biofilm and their visible light activity. Nanoscale **5**, 6323–6326 (2013)

33. Vijayakumar, S., Ponnalagi, A., Nagamuthu, S., Muralidharan, G.: Microwave assisted synthesis of Co$_3$O$_4$ nanoparticles for high-performance super capacitors. Electrochem. Actam **106**, 500 (2013)

34. Lopez, Rosendo, Gomez, Ricardo: Band-gap energy estimation from diffuse reflectance measurements on sol–gel and commercial TiO2: a comparative study. J. Sol-Gel. Sci. Technol. **61**, 1–7 (2012)

35. Saha, B., Das, S., Chattopadhyay, K.K.: Electrical and optical properties of Al doped cadmium oxide thin films deposited by radio frequency magnetron sputtering. Solar Energy Mater. Sol. Cel. **91**, 1692–1697 (2007)

36. Zang, C.H., Zhang, D.M., Tang, C.J., Fang, S.J., Zong, Z.J., Yang, Y.X., Zhao, C.H., Zhang, Y.S.: Optical properties of a ZnO/P nanostructure fabricated by a chemical vapor deposition method. J. Phys. Chem. C **113**, 18527–18530 (2009)

37. Zhuge, L.J., Wu, X.M., Wu, Z.F., Yang, X.M., Chen, X.M., Chen, Q.: Structure and deep ultraviolet emission of Co-doped ZnO films with Co3O4 nano-clusters. Mater. Chem. Phys. **120**, 480–483 (2010)

38. Yang, J., Gao, M., Yang, L., Zhang, Y., Lang, J., Wang, D., Wang, Y., Liu, H., Fan, H.: Low-temperature growth and optical properties of Ce-doped ZnO nanorods. Appl. Surf. Sci. **255**, 2646–2650 (2008)

39. Malleshappa, J., Nagabhushana, H., Sharma, S.C., Vidya, Y.S., Anantharaju, K.S., Prashantha, S.C., Daruka Prasad, B., Raja Naika, H., Lingaraju, K., Surendra, B.S.: Leucas aspera mediated multifunctional CeO$_2$ nanoparticles: structural, photoluminescent, photocatalytic and antibacterial properties. Spectrochim. Acta Part A Mol. Biomol. Spectrosc. **149**, 452–462 (2015)

40. Naika, R., Prashantha, S.C., Nagabhushana, H., Sharma, S.C., Nagabhushana, B.M., Nagaswarupa, H.P., Premkumar, H.B.: Low temperature synthesis and photoluminescence properties of red emitting Mg$_2$SiO$_4$:Eu$^{3+}$ nanophosphor for near UV light emitting diodes. Sens. Actuators B: Chem. **195**, 140–149 (2014)

41. Wang, Yanbin, Zhao, Hongying, Li, Mingfang, Fan, Jiaqi, Zhao, Guohua: Magnetic ordered mesoporous copper ferrite as a heterogeneous, Fenton catalyst for the degradation of imidacloprid. Appl. Catalys. B: Environ. **147**, 534–545 (2014)

42. Ren, Ao, Liu, Chunbo, Hong, Yuanzhi, Shi, Weidong, Lin, Shuang: Ping Li., Enhanced visible-light-driven photocatalytic activity for antibiotic degradation using magnetic NiFe$_2$O$_4$/Bi$_2$O$_3$ hetero structures. J Chem. Eng. **258**, 301–308 (2014)

43. Jing, Panpan, Li, Jianan, Pan, Lining, Wang, Jianbo, Sun, Xiaojun, Liu, Qingfang: Efficient photocatalytic degradation of acid fuchsine in aqueous solution using separate porous tetragonal-CuFe2O4 nanotubes. J. Hazard. Mater. **284**, 163–170 (2015)

44. Wanga, Yanbin, Zhaob, Hongying, Zhao, Guohua: Iron-copper bimetallic nanoparticles embedded within ordered mesoporous carbon as effective and stable heterogeneous Fenton catalyst for the degradation of organic contaminants. Appl. Catal. B **164**, 396–406 (2015)

Springer